

Interlayer properties of tungsten fibre-reinforced composites and their determination by different methods[☆]

H. Gietl^{a,*}, J. Riesch^{b,*}, M. Zielinski^b, T. Höschen^b, J.W. Coenen^{c,d}, S. Schönen^c, R. Neu^{b,e}

^a Materials Science and Technology Division, Oak Ridge National Laboratory, Oak Ridge, TN, 37831, USA

^b Max-Planck-Institut für Plasmaphysik, Boltzmannstrasse 2, 85748 Garching, Germany

^c Forschungszentrum Jülich GmbH, Institut für Energie und Klimaforschung, Partner of the Trilateral Euregio Cluster (TEC), 52425 Jülich, Germany

^d Department of engineering physics, University of Wisconsin Madison, WI 53706 Madison, USA

^e Technische Universität München, Boltzmannstrasse 15, 85748 Garching, Germany

ARTICLE INFO

Keywords:

Metal–matrix composites (MMCs)
Interface/interphase
Mechanical properties/testing

ABSTRACT

Tungsten features a unique combination of properties which makes it a candidate for the use as a plasma-facing material in fusion reactors. The main drawbacks of tungsten are its brittleness at moderate temperature and the susceptibility to embrittlement during operation. To overcome this limitations tungsten fibre-reinforced tungsten composites (W_f/W) have been developed. The interlayer between the tungsten fibre and tungsten matrix enables the activation of extrinsic mechanisms to improve the toughness similar to ceramic fibre-reinforced ceramics. In addition, the evaluation of the interlayer parameter is a necessary for the efforts to model the composite behaviour. Therefore, single fibre model systems with Er_2O_3 and Y_2O_3 as interlayer were evaluated by push-out and pull-out tests. The results were used to determine the interfacial shear strength (τ_{deb}), the interfacial frictional shear stress (τ_{fr}) and the fracture energy of the interlayer (G_I). In addition, tensile tests on the composite material were performed to evaluate the interfacial frictional shear stress. The evaluation methods were critically discussed as the results show that the influence of the evaluation method is larger than the actual tested interlayer material.

1. Introduction

Due to its unique properties such as low sputter yield, high melting point and moderate activation, tungsten (W) is the most promising candidate for the use as a plasma facing material in a future fusion device [1]. The inherent brittleness below the ductile-to-brittle transition temperature (DBTT) [2,3] and the embrittlement during operation, e.g. by overheating [4] and/or neutron irradiation [5,6] are the main drawbacks for the use of pure W. The brittleness is mitigated in tungsten fibre-reinforced tungsten composites (W_f/W) [7–9] which utilize extrinsic mechanisms to improve the toughness similar to ceramic fibre-reinforced ceramics [10]. During the development process of W_f/W all constituents of the composite, which are fibre [11,12], interface between fibre and matrix [13,14] and matrix fabrication [15,16] were addressed. It has been shown that the toughening in principle works in

the as-fabricated state as well as after embrittlement by high temperature annealing [17,18]. W_f/W shows at room temperature in bending tests typically stable crack propagation and a increased fracture toughness compared to pure W [18]. One essential requirement to increase the toughness in a brittle matrix composite is that the interlayer enables fibre–matrix debonding. Hence, the behaviour of the interlayer is crucial for the load bearing capability of the composite. In addition, the evaluation of reliable interlayer parameters is mandatory for the overall composite modelling efforts and thus different load directions are of interest [19].

Several push-out studies of W_f/W have already been performed in the past [14,20–22]. For that studies a single fibre model system consist of a single W fibre which was coated with a interlayer material and then ingrown into a dense W matrix was developed. The previous push-out results do not show a significant influence of different interlayer

[☆] Notice: This manuscript has been authored by UT-Battelle, LLC, under contract DE-AC05-00OR22725 with the US Department of Energy (DOE). The US government retains and the publisher, by accepting the article for publication, acknowledges that the US government retains a nonexclusive, paid-up, irrevocable, worldwide license to publish or reproduce the published form of this manuscript, or allow others to do so, for US government purposes. DOE will provide public access to these results of federally sponsored research in accordance with the DOE Public Access Plan (<http://energy.gov/downloads/doe-public-access-plan>).

* Corresponding authors.

E-mail addresses: gietlha@ornl.gov (H. Gietl), johann.riesch@ipp.mpg.de (J. Riesch).

¹ Former affiliations: Max-Planck-Institut für Plasmaphysik, Boltzmannstrasse 2, 85748 Garching, Germany & Technische Universität München, Boltzmannstrasse 15, 85748 Garching, Germany.

materials [13] and so we assume here that the test method has a larger influence than the actually used interlayer material. This hypothesis motivated this comparative study and the development of new testing methods. A new single fibre composite testing method for W_f/W is the single fibre pull-out tests where a fibre is pulled out of the matrix. This allows the evaluate of the interlayer behaviour under tensile load which is in contrast to the compression load state during push-out testing. From the pull-out and push-out test on single fibre composites model systems with two different interlayer materials (Er_2O_3 and Y_2O_3) the interfacial shear strength (τ_{deb}), the interfacial frictional shear stress (τ_{fr}) and the fracture energy of the interlayer (Γ_f) were calculated. These are important parameters for the damage tolerance of composites [10]. Furthermore, τ_{fr} was evaluated from tensile test results with multiple matrix cracking. The influence of the three different evaluation methods are critically discussed and set in context for the further development of W_f/W .

2. Material

2.1. W fibres

Potassium (K) doped drawn tungsten wires with a diameter of 150 μm were provided by the OSRAM GmbH, Schwabmünchen and will be called W fibres (W_f) in the following. W fibres with a diameter of 150 μm are ductile at room temperature with a strength up to ≈ 2700 MPa [12]. The Poisson ratio (ν_f) and Young's modulus (E_f) of the W_f is similar to bulk W with 0.28 and 400 GPa, respectively [3]. Once the W_f is annealed at 1900 $^{\circ}C$ for 0.5 h it still has some ductility while annealing at 2300 $^{\circ}C$ for 0.5 h leads to a complete brittle fracture [12]. This results in a significant reduced Γ_f after annealing to 2300 $^{\circ}C$ for 0.5 h. In contrast to that, pure W fibre after annealing to 1627 $^{\circ}C$ show brittle fracture [23]. The specific fracture energy of the W_f after different heat treatments is shown in Table 1.

2.2. Interlayer production

Two different interlayers with a thickness of 1 μm were deposited on the isopropanol cleaned fibre surface with reactive magnetron sputtering by using a 99.9% pure erbium or yttrium target, respectively. The interlayer coating was performed in a two step depositions processes with a process interruption to turn the fibre (see Section 2.3). The parameters for the erbia deposition are chosen according to [13] and yttria was deposited according to [9].

2.3. Model systems

To minimize the influence of manufacturing on the results, the samples with the same interlayer were manufactured in one batch. At first, the W fibre (see Section 2.1) was wound on a copper frame. This set up was then cleaned with acetone and isopropanol in a ultrasonic bath for 10 min each. Once the fibre was coated with the interlayer (see Section 2.2), the copper frame with the fibre was clamped together with two copper plates and a stainless steel cap with gas inlet. A technical drawing of the set up is showing in the attachment (Fig. A.1). This setup was placed in the vacuum chamber of a CVD deposition furnace (WILMA [24]). Tungsten hexafluoride and hydrogen as precursor gas at a deposition temperature of 600 $^{\circ}C$ was used to grow the W matrix with a thickness of 2 mm on the fibres [25]. The set up after CVD W deposition with the removed upper stainless steel cap (cut with electrical discharge machining (EDM)) is shown in Fig. 1 (a). In the next step the single fibre composite sticks were cut out with EDM. In Fig. 1 (b) one single fibre composite with the holder for final sample cutting is shown.

The overall length of the cut specimens was 120 mm which includes a 40 mm single fibre W_f/W composite in the middle and two 40 mm free fibre ends on either side (see Fig. 1 (b)). To produce pull-out test

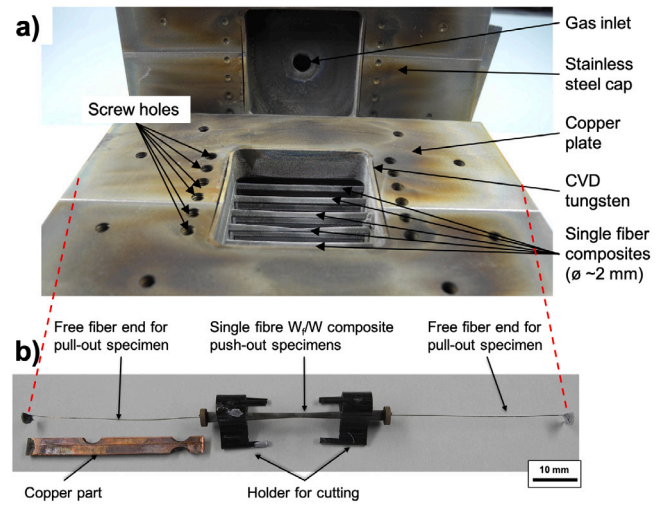


Fig. 1. (a) Set up for the production of single fibre composites after the first cut with EDM to remove the upper stainless steel cap and (b) single fibre composite stick with the holder for final sample cutting. The pull-out and push-out specimens are fabricated out of the same single fibre composite.

specimens as seen in Fig. 3 (b) the W_f/W sticks were cut with a diamond wire saw and then polished to the desired specimen thickness which varies from 100 to 700 μm . As there are two free fibre ends, two pull-out specimens per stick were produced. Afterwards, the remaining stick was sliced with a diamond saw and these disks were polished on both sides to get the push-out specimens with the desired thickness between 75 to 300 μm as described in [21].

2.4. Composite material

The bulk W_f/W material investigated in this work was produced with a layerwise chemical vapour deposition process as described previously [26]. Two different composite types were produced. The first composite had pure W fibres with a diameter of 150 μm [23] coated with a 1 μm erbium oxide interlayer. The fibres were unidirectional aligned with a uniform fibre distance of around 120 μm . The fibre volume fraction was $\approx 22\%$ and the density was 94%. According to the interlayer material the first composite is called $W_f/W_{Er_2O_3}$ in the following. The second composite type was produced using W fabrics [15] consisting of 150 μm diameter K doped W fibres as warp fibre and 50 μm as weft fibre with a uniform fibre distance of ≈ 230 μm . The fabrics were coated with a 1 μm yttria interlayer. According to the interlayer material the second composite is named $W_f/W_{Y_2O_3}$ in the following. $W_f/W_{Y_2O_3}$ had a fibre volume ratio of 11% and a density of 99.3%. All specimens were machined with EDM and polished at all sides to get the tensile specimen geometry presented in [26].

3. Method

All tests were performed with an universal testing device (TIRAtest 2820, Nr. R050/01, TIRA GmbH) at room temperature (RT) on air.

3.1. Testing of model systems

3.1.1. Testing: Push-out

The universal testing device was equipped with an instrumented macroindentation system using a 200 N load cell for the push-out test. These tests were performed analogous to previous tests by Du et al. [14,20,21]. The polished push-out samples were positioned in a sample holder so that the fibre is exactly above a small hole (diameter ≈ 350 μm). The tungsten carbide indenter with a diameter of 120 μm

Table 1
 Γ_f of W fibres after different heat treatment [11,12,23].

	W_f as-fabricated	W_f annealed 1900 °C for 0.5 h	W_f annealed 2300 °C for 0.5 h	Pure W_f annealed 1627 °C for 0.5 h
Γ_f	$1.2 \cdot 10^6$ [J/m ²]	$9.4 \cdot 10^5$ [J/m ²]	$2.3 \cdot 10^4$ [J/m ²]	$1.28 \cdot 10^4$ [J/m ²]

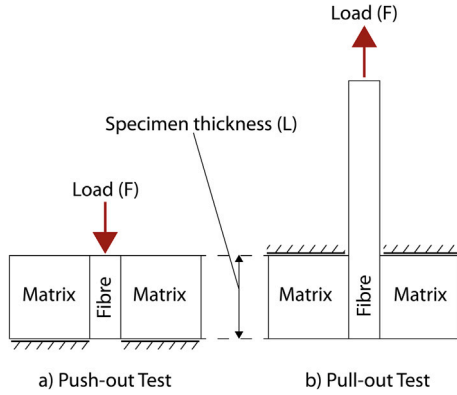


Fig. 2. Schematic of (a) push-out (sample holder on bottom of specimen) and (b) pull-out test (sample holder on top of specimen).

was moved with a constant cross head displacement of 1 $\mu\text{m/s}$ to push the fibre out of the specimen. The cross head displacement and force were recorded over time. From previous studies on W_f/W [13,22] it is known, that the samples which are used for our push-out equipment must have a thickness below 320 μm . If the samples are thicker, the needed push-out force gets too high and the indenter fails. The thickness of the specimens were measured before the test and varied from 74 to 311 μm . A sketch of a single fibre push-out test is shown in Fig. 2 (a) where the specimen is placed on the holder and pushed out with a load (F).

3.1.2. Testing: Pull-out

A schematically image of the pull-out set up is shown in Fig. 2 (b). During the pull-out test a free fibre end is pulled out of a matrix while the matrix is hold down and thus fixed. In Fig. 3 (a) the assembled pull-out set up in the universal testing device and in Fig. 3 (b) one pull-out sample is shown. The free fibre end of the specimen was clamped into a holder (Fig. 3 (a)). Then the fibre was placed in the slot of the holding down clamp (slot width 200 μm) which enables the fibre movement in vertical direction. To ensure an uniaxial stress on the specimen the sample was pre-loaded with 2 N and by moving the x-y-table aligned by minimizing the load. The fibre was pulled out of the matrix by moving the holder upwards with a cross head displacement of 5 $\mu\text{m/s}$. The cross head displacement, time and force (200 N load cell) were recorded. The free fibre length was ≈ 40 mm. The maximum thickness for the pull-out specimen was determined during preliminary tests to values below 750 μm . At that thickness, the pull-out load is still in the elastically region of the 150 μm W fibre (below 45 N) [11,12]. The specimen thickness, which was measured before the test, varied from 110 to 721 μm .

3.1.3. Interlayer parameters of model systems

Based on several theoretical models [27–32] a nonlinear regression curve fitting method utilizing the experimental push-out and pull-out test results was used to evaluate the interfacial properties. This analysis was also used by Du et al. [13,21]. For a quantitative identification of the interfacial shear resistance, the interfacial shear strength τ_{deb} is defined as the maximum average shear stress the interfaces could withstand immediately before it begins to fail. For the calculation of τ_{deb} the debonding force (F_{deb}) denotes the applied load at the moment the interlayer debonds [33]. Gresczuk [27] formulated a relationship

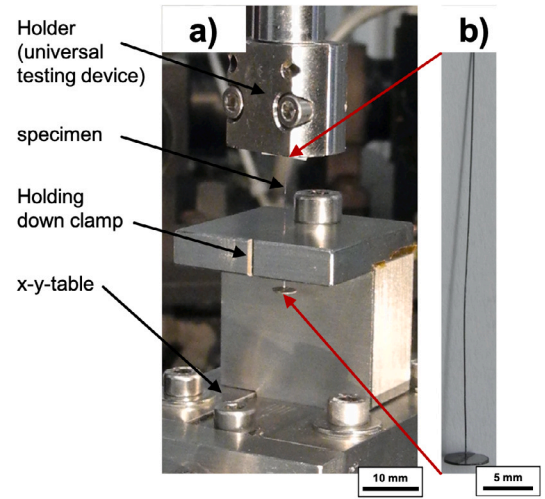


Fig. 3. Pull-out test equipment: (a) overview of the pull-out test set up with holder (upper clamp), specimen, holding down clamp and x-y-table; (b) detailed view of one pull-out specimen.

between the debonding load F_{deb} and the debonding shear strength τ_{deb} based on the shear-lag theory of pull-out test.

$$F_{deb} = \frac{\pi \cdot d \cdot \tau_{deb}}{\alpha} \tanh(\alpha \cdot L) \quad (1)$$

where τ_{deb} is the interfacial bond shear strength, α is a constant which depends on the fibre–matrix geometry as well as on the elastic properties of the fibres and matrix, d is the fibre diameter and L is the specimen thickness according to Fig. 2(a), (b). The interfacial frictional shear stress τ_{fr} which is determined by the interfacial friction coefficient μ and the interfacial radial stress σ_R , according to the Coulomb law with $\tau_{fr} = \sigma_R \cdot \mu$. σ_R is defined as the radial stress oriented normal to the interface caused by the roughness mismatch of separated surfaces during the sliding movement of a fibre. Based on a theoretical model, σ_R and μ can be calculated with the following equation [31].

$$F_{fr-push-out} = \frac{\pi \cdot d_f^2 \cdot \sigma_R}{4 \cdot k} \left[\exp\left(\frac{4 \cdot \mu \cdot k \cdot L}{d_f}\right) - 1 \right] \quad (2)$$

By consequential following the procedure of Shetty [31] for the development of the push-out evaluation one can use the modified Eq. (3) for the evaluation of the pull-out test.

$$F_{fr-pull-out} = \frac{\pi \cdot d_f^2 \cdot \sigma_R}{4 \cdot k} \left[1 - \exp\left(-\frac{4 \cdot \mu \cdot k \cdot L}{d_f}\right) \right] \quad (3)$$

where F_{fr} is called frictional force, which is the peak friction load in the push-out and pull-out curve (see in Figs. 4 and 9). The dimensionless elastic parameter $k = E_m \nu_f / [E_m(1 - \nu_f) + E_f(1 + \nu_m)]$ is related to the Poisson ratio (ν) and Young's modulus (E). The subscripts f and m indicate fibre and matrix which is equal for our case as the fibre and matrix are W ($\nu = 0.28$ [3] and $E = 400$ GPa [3] $\Rightarrow k = 0.14$). Thus σ_R and μ can be fitted using experimental $F_{fr}-L$ data with Eq. (2) (push-out) or Eq. (3) (pull-out). The last parameter of interest is the interfacial fracture energy Γ_i , which is defined as the critical energy release rate required for interfacial debonding. This parameter will be used to calculate the debonding criteria $D = \Gamma_i / \Gamma_f$. Liang et al. [32] developed based on the pull-out model of Hutchinson et al. [34] the

following theoretical model for the evaluation of Γ_i for push-out test which takes the F_{deb} into account.

$$F_{deb-push-out} = \left[2\sqrt{\frac{2 \cdot \Gamma_i \cdot E_f}{B_2 \cdot d}} e^{\xi} + \frac{\tau_R}{\mu \cdot B_1} (e^{\xi} - 1) \right] \cdot \frac{\pi \cdot d^2}{4} \quad (4)$$

By consequential following the procedure of Liang et al. [32] for the development of the push-out evaluation one can use the modified Eq. (5) for the evaluation of the pull-out test.

$$F_{deb-pull-out} = \left[2\sqrt{\frac{2 \cdot \Gamma_i \cdot E_f}{B_2 \cdot d}} e^{-\xi} + \frac{\tau_R}{\mu \cdot B_1} (1 - e^{-\xi}) \right] \cdot \frac{\pi \cdot d^2}{4} \quad (5)$$

where, $\xi = \mu B_1 L/d$, $B_1 = k = E_m \nu_f / [E_m (1 - \nu_f) + E_f (1 + \nu_m)] = 0.14$, and $B_2 = 1 - 2\nu_f B_1 = 0.9216$. To obtain Γ_i , F_{deb} -L data are fitted with Eq. (4) (push-out) and Eq. (5) (pull-out). As Eqs. (2) and (4), and thus also Eqs. (3) and (5) are mutually related, the curve fitting for Γ_i , σ_R and μ were performed simultaneously based on maximum likelihood via Monte-Carlo Markov chain [35].

3.2. Testing of the composite

3.2.1. Tensile test

Besides testing of model system, the interfacial frictional shear stress can be evaluated with tensile tests by analysing of this multiple matrix cracking (see Section 3.2.2). The tensile test results of $W_f/W_{Er_2O_3}$ were already published [26] and the specimens were now again reviewed with regards to multiple matrix cracking. The tensile tests for $W_f/W_{Y_2O_3}$ are performed similar to the previously reported tensile test. A displacement rate of $10 \mu\text{m/s}$ was used and the force was measured with a 20 kN load cell. A holding system where the specimens were inserted into holders without clamping was used to avoid stress peaks at the contact surface. The holders were mounted by chains to the universal testing device to allow self alignment and thus an uniaxial stress-state within the specimen. A detailed description of the tension test setup and results for $W_f/W_{Er_2O_3}$ can be found in [26]. For the $W_f/W_{Y_2O_3}$ specimens, the load-displacement curves were correlated with an optical measurement system for real time displacement and cracking observation which was not available for the $W_f/W_{Er_2O_3}$ specimens in the previous work where the corrected cross head displacement was used.

3.2.2. Evaluation of composite material: multiple matrix cracking

A composite which withstands the initial matrix crack shows multiple matrix cracks until complete fracture [36]. This behaviour is known as multiple matrix cracking of brittle matrix composites [37]. The matrix is already cracked several times, and thus the ultimate tensile strength of the composite is related to the fibre strength and fibre volume fraction. In such a composite the fibre has the possibility to debond from the interlayer [38]. The matrix cracks are evenly distributed over the whole tensile specimen. The distance between the matrix cracks is defined by the interfacial frictional shear stress [37,39]. So, the interfacial frictional shear stress τ_{fr} can be calculated by taking the distances between the matrix cracks into account [36,40,41].

Aveston et al. [36,39] established the theory for multiple matrix cracking in brittle matrix composites. These equations are based on the assumption that the fibres bridges the crack if the matrix is cracked and these fibres are not longer bonded to the matrix but the load is transferred with a constant interfacial frictional shear stress. The energy balance analysis showed that the onset of matrix cracking occurs at stresses greater than:

$$\sigma^* = \left[\frac{6 \cdot \tau_{re} \cdot \Gamma_m \cdot f^2 \cdot E_f \cdot E_c^2}{(1 - f) \cdot E_m^2 \cdot r} \right]^{1/3} \quad (6)$$

With τ_{re} the interfacial frictional shear stress, Γ_m fracture energy of the matrix, f the fibre volume fraction, E_m the matrix modulus of

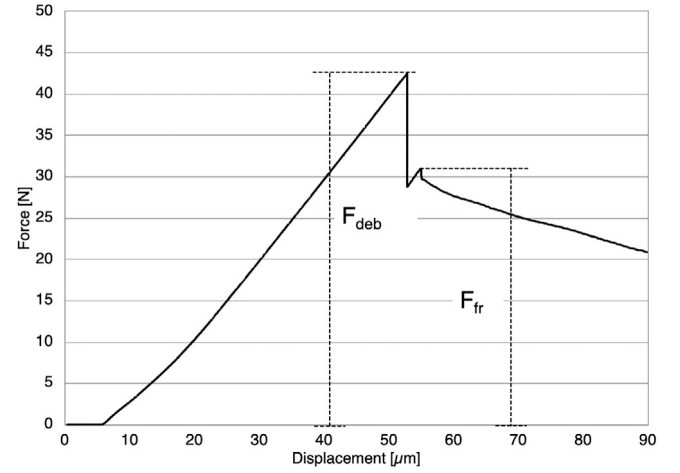


Fig. 4. Representative curve of a push-out specimen with Er_2O_3 interlayer and a specimen thickness of $238 \mu\text{m}$. A linear loading followed by a load drop and the final fibre push-out against friction is shown. The debonding (F_{deb}) and frictional force (F_{fr}) which will be used for the calculations are marked.

elasticity, E_f as fibre modulus of elasticity, E_c the composite modulus of elasticity defined by $E_c = f \cdot E_f + (1 - f) E_m$ and r the fibre radius.

Since matrix cracking does not occur at a exact defined stress level and the real fracture energy of the matrix is not known, simple multiple fracture theory cannot be used to calculate τ_{re} . Instead, it was assumed that the matrix cracking follows a Weibull distribution function as presented by Curtin [37] to determine τ_{re} . This results in the following equation:

$$\tau_{re} = \frac{(1 - f) \cdot E_m}{f \cdot E_c} \cdot \frac{r \cdot \sigma_{cs}}{2\bar{l}} \cdot \Lambda(m, \sigma_{cs}/\sigma^*) \quad (7)$$

With σ_{cs} is a characteristic stress (63.2% probability level), \bar{l} is the average crack spacing, $\Lambda(m, \sigma_{cs}/\sigma^*)$ is a function of the Weibull modulus, m and σ_{cs}/σ^* where σ^* is the stress at which the first matrix crack occurs [37].

4. Results

4.1. Push-out

4.1.1. Interlayer evaluation

Push-out tests were performed for 30 samples with Er_2O_3 and 31 samples with Y_2O_3 interlayer. In Fig. 4, a representative push-out curve from a Er_2O_3 samples with a specimen thickness of $238 \mu\text{m}$ is shown. The Y_2O_3 samples showed a similar behaviour. First, the measured load is zero as the indenter is not touching the sample yet. The curve then shows a linear increase until the maximum load is reached. Followed by a load drop, which is according to literature [42] caused by the complete debonding of the interlayer. Subsequently, the fibre is pushed out from the matrix against the frictional force of the interlayer. It is also shown how the debonding (F_{deb}) and frictional force (F_{fr}) was evaluated from the force-displacement curves.

The results of the debonding force as function of the specimen thickness are shown in Fig. 5.

With Eq. (1), the interfacial shear strength τ_{deb} was calculated to the following values.

- Er_2O_3 debonding: $\tau_{deb-push-\text{Er}_2\text{O}_3} = 356.2 \pm 4.8 \text{ MPa}$
- Y_2O_3 debonding: $\tau_{deb-push-\text{Y}_2\text{O}_3} = 447.3 \pm 2.2 \text{ MPa}$

The frictional force as function of the specimen thickness is shown in Fig. 6.

τ_{fr} was calculated by simultaneous curve fitting of Eqs. (2) and (4) to the following values:

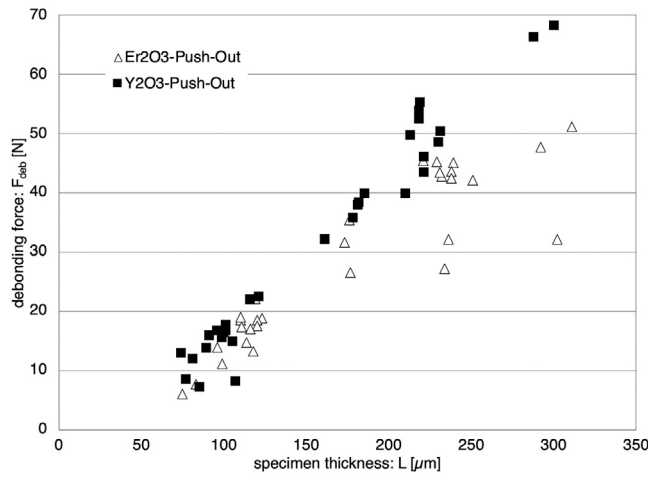


Fig. 5. Debonding force evaluated from the push-out tests. With increasing specimen thickness the debonding force is increasing. A small differences between the two interlayer materials are visible for thicker specimens while thin specimens show neglectable differences.

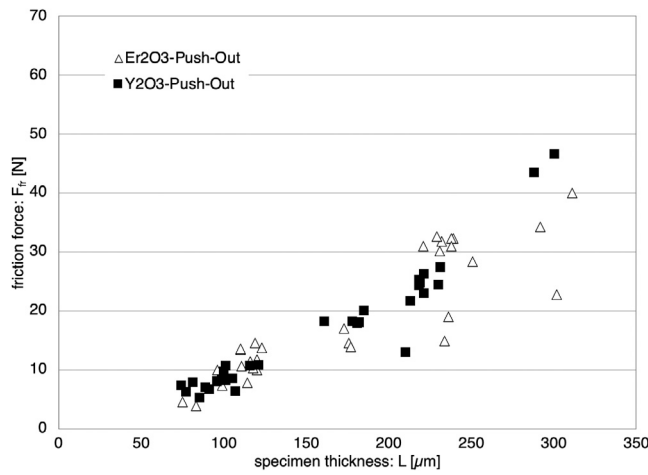


Fig. 6. Frictional force of the push-out tests. With increasing specimen thickness the frictional force is increasing. Only minor difference between the two different interlayer materials are visible for thicker specimens.

- Er_2O_3 friction: $\tau_{fr-push-\text{Er}_2\text{O}_3} = 180.2 \pm 21.3 \text{ MPa}$
- Y_2O_3 friction: $\tau_{fr-push-\text{Y}_2\text{O}_3} = 124.6 \pm 6.0 \text{ MPa}$

The specific fracture energies were calculated with Eqs. (2) and (4) to the following values.

- Er_2O_3 specific fracture energy: $\Gamma_{i-push-\text{Er}_2\text{O}_3} = 5.2 \pm 0.3 \text{ J/m}^2$
- Y_2O_3 specific fracture energy: $\Gamma_{i-push-\text{Y}_2\text{O}_3} = 5.0 \pm 0.2 \text{ J/m}^2$

4.1.2. Fracture surface

For the evaluation of the interlayer after the push-out test, two specimen per interlayer material were polished till the middle of specimen was reached. This preparation procedure allowed the investigation of the interlayer over the entire specimen thickness. In Figs. 7 and 8 longitudinal polished sections after the test are shown.

Fig. 7 shows a 232 μm thick sample with a Er_2O_3 interlayer which had a debonding force of 42.8 N. Fig. 7 (a) shows the overview image of the sample. Fig. 7 (b), (c), (d) and (e) are detail pictures of the interlayer. In the images with higher magnification, the horizontal W grains of the CVD matrix and the elongated vertical W grains in the fibre resulting from the wire drawing are visible. The interlayer

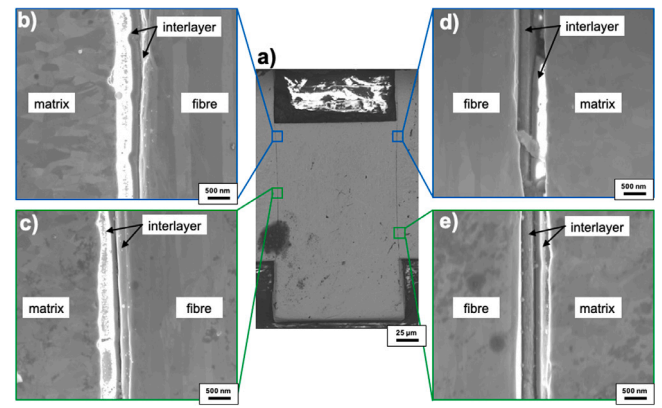


Fig. 7. Cross section of a push-out specimen with Er_2O_3 interlayer (L: 232 μm , F_{deb} : 42.8 N) (a) SEM overview image, (b)–(e) detailed view of interlayer. The debonding for this specimen took place within the Er_2O_3 layer. (The different appearance of the two interlayer parts is related to charging caused by epoxy impurities on the interlayer surface).

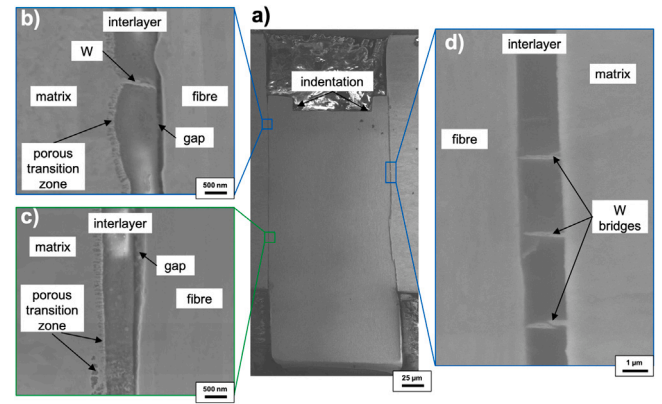


Fig. 8. Cross section of a push-out specimen with Y_2O_3 (L: 300 μm , F_{deb} : 68.3 N) (a) SEM overview image, (b)–(d) detailed view of interlayer. The debonding for this specimen took place on the fibre surface and the Y_2O_3 layer is undamaged.

is noticeable between the fibre and the matrix. The thickness of the interlayer of this specimen is between 0.7 – 1.0 μm . In all images (see Fig. 7 (b) – (e)) a similar interlayer structure can be observed for this specimen. The interlayer remains connected to the matrix and the fibre after the test. The failure takes place within the interlayer. In the upper part of Fig. 7 (d) a piece of the interlayer is missing.

In Fig. 8 a cross section of a specimen with Y_2O_3 is shown. This sample has a thickness of 300 μm corresponds to a debonding force of 68.3 N. Fig. 8 (b), (c), (d) and (e) shows a detailed view of the 0.8 – 1.2 μm thick interlayer.

In the overview figure (Fig. 8 (a)) an indentation of the indenter into the fibre is visible. In Fig. 8 (b) and (c), a porous transition zone between the interlayer to the W matrix is visible. On both sides, W bridges (confirmed with energy dispersive X-ray spectroscopy (EDS)) between fibre and matrix were found (see Fig. 8 (b) and (d)). Such W bridges were found over the entire length of the interlayer. In Fig. 8 (b) and (c) a gap between fibre and the interlayer is visible. This indicates that the interlayer is still attached to the matrix and has debonded from the fibre. That shows for this sample, that the adhesion between the matrix and the interlayer is stronger than between the interlayer and the fibre.

Only one specimen per interlayer material was investigated in that way, but as the force–displacement behaviour of all specimens was comparable we assume that the all the materials behaved the same in regard to the debonding region.

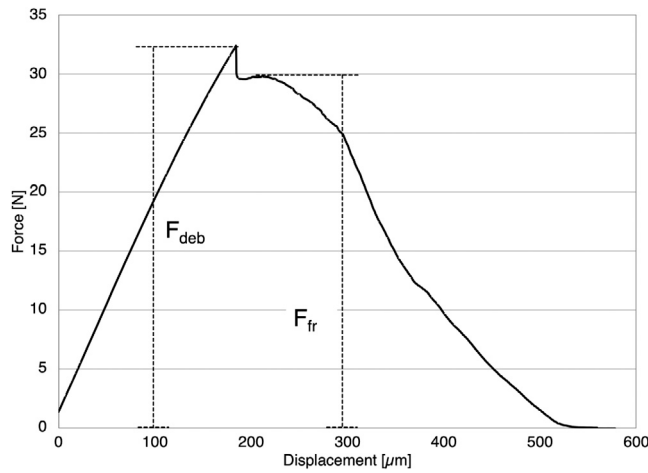


Fig. 9. Representative curve of a pull-out specimen with an Er_2O_3 interlayer and a specimen thickness of 423 μm . A linear loading is followed by a load drop and a decreasing load until zero (complete fibre pull-out). The debonding (F_{deb}) and frictional force (F_{fr}) which will be used for the calculations are marked.

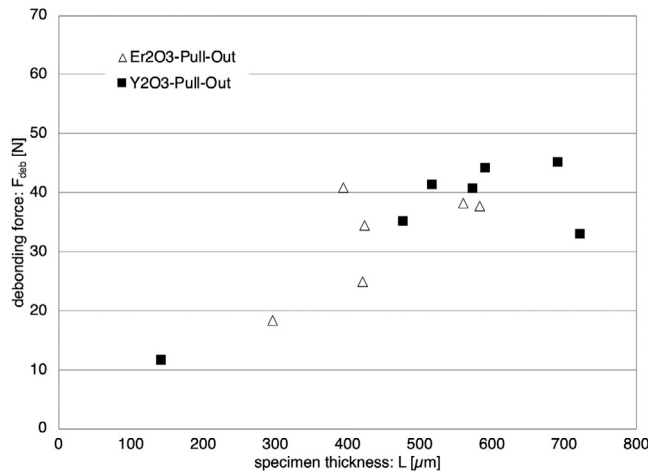


Fig. 10. Debonding forces determined by pull-out tests. With increasing specimen thickness the debonding force is increasing. The different materials show comparable results for comparable thicknesses. However, no thick or thin specimens could be tested for Er_2O_3 and thus only a minor overlapping thickness region can be observed.

4.2. Pull-out

4.2.1. Interlayer evaluation

6 samples with Er_2O_3 and 7 samples with Y_2O_3 interlayer were tested successfully. The behaviour of both interlayer materials was similar. Fig. 9 shows a representative curve of a sample with a thickness of 423 μm and a Er_2O_3 interlayer.

The curve shows a linear behaviour until the maximum force is reached. This is followed by a load drop, which is according to literature [42] caused by the complete debonding of the interlayer. Subsequently, the fibre is pulled out of the matrix against the frictional force of the interlayer. In Fig. 9 it is shown how the debonding force (F_{deb}) and the frictional force (F_{fr}) are determined from the load-displacement curve. The debonding forces over the specimen thicknesses for all tested samples are shown in Fig. 10.

The interfacial shear strength τ_{deb} was calculated with Eq. (1) to the following values.

- Er_2O_3 debonding: $\tau_{deb-pull-\text{Er}_2\text{O}_3} = 187.3 \pm 7.9$ MPa
- Y_2O_3 debonding: $\tau_{deb-pull-\text{Y}_2\text{O}_3} = 238.3 \pm 11.0$ MPa

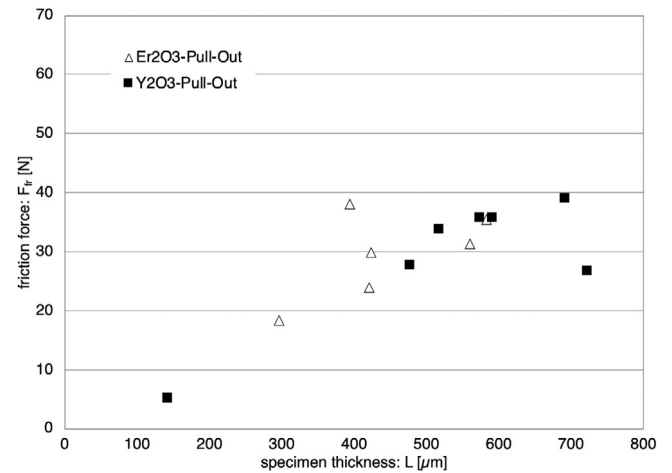


Fig. 11. Frictional forces determined by pull-out tests. The frictional force is increasing up to a specimen thickness of ≈ 500 μm and is then approximately constant. The different materials show comparable results for comparable thicknesses. However, no thick or thin specimens could be tested for Er_2O_3 and thus only a minor overlapping thickness region can be observed.

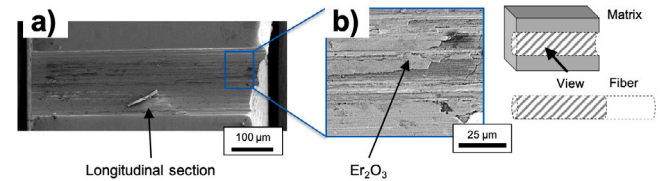


Fig. 12. Cross-section of the matrix of a pull-out sample with a Er_2O_3 interlayer after the test (L: 583 μm , F_{deb} : 37.7 N) (a) SEM overview image (b) SEM detail image of the interlayer region. Some Er_2O_3 was visible in the matrix where the fibre was pulled out.

A summary of the frictional force over the specimen thickness for all specimens are shown in Fig. 11.

τ_{fr} for both interlayers were calculated with Eqs. (2) and (4) to the following values:

- Er_2O_3 friction: $\tau_{fr-pull-\text{Er}_2\text{O}_3} = 154.6 \pm 44$ MPa
- Y_2O_3 friction: $\tau_{fr-pull-\text{Y}_2\text{O}_3} = 166.6 \pm 23$ MPa

The specific fracture energies for Er_2O_3 and Y_2O_3 were calculated with Eqs. (2) and (4) the following values:

- Er_2O_3 specific fracture energy: $\Gamma_{i-push-\text{Er}_2\text{O}_3} = 3.0 \pm 0.65$ J/m²
- Y_2O_3 specific fracture energy: $\Gamma_{i-push-\text{Y}_2\text{O}_3} = 13.0 \pm 0.67$ J/m²

4.2.2. Fracture surface

SEM images of a polished longitudinal section of the matrix from which a fibre was pulled out are shown in Fig. 12(a) and (b). In Fig. 12 (b) Er_2O_3 (confirmed with EDS) is detected on the matrix.

In Fig. 13 (a), (b) and (c) the extracted fibre (corresponding matrix see Fig. 12) is shown. The transition from matrix to free fibre in Fig. 13 (c) is marked with a black dashed line. On the surface (see Fig. 13 (b) and (c)) which was embedded in the matrix, Er_2O_3 flakes (confirmed by EDS) are distributed over the entire fibre surface. Some of the Er_2O_3 flakes are marked in Fig. 13 (c).

In Fig. 14 SEM images of a polished cross section of the matrix after the fibre pull-out with Y_2O_3 interlayer is shown. In Fig. 14 (b) Y_2O_3 , which is attached to matrix was confirmed with EDS. The Y_2O_3 which is visible in Fig. 14 (b) has a rough structured surface.

Fig. 15 (a), (b) and (c) shows the fibre after the pulled out of the matrix. The transition from the embedded to the free fibre end

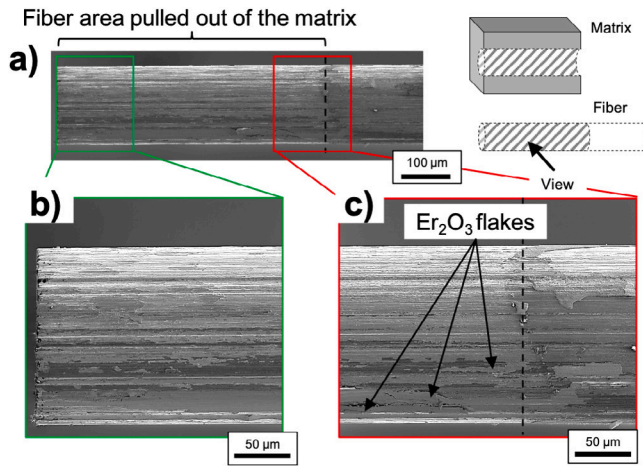


Fig. 13. Fibre which was pulled out of a specimen with Er_2O_3 interlayer (L : 583 μm , F_{deb} : 37.7 N) (a) SEM overview image (b), (c) SEM detailed view of the fibre. Some Er_2O_3 was visible in the fibre which was pulled out of the matrix. This indicates in combination with the findings from Fig. 12 indicates that Er_2O_3 failed within the interlayer.

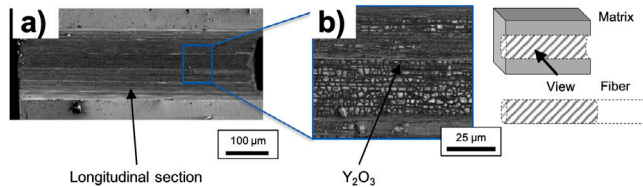


Fig. 14. Cross-section of the matrix of a pull-out sample with a Y_2O_3 interlayer after the test (L : 591 μm , F_{deb} : 44.3 N) (a) SEM overview image (b) SEM detail image of the interlayer region. Over the entire matrix where the fibre was pulled out a rough structured layer of Y_2O_3 is visible.

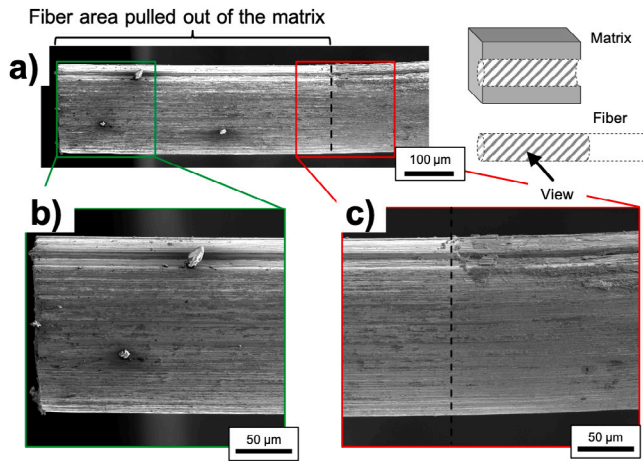


Fig. 15. Fibre which was pulled out of a specimen with Y_2O_3 interlayer (L : 591 μm , F_{deb} : 44.3 N) (a) SEM overview image (b), (c) SEM detailed view of the fibre. No Y_2O_3 was visible in the fibre which was pulled out of the matrix. This indicates in combination with the findings from Fig. 14 indicates that Y_2O_3 failed on the fibre surface and it was stuck to the matrix.

is marked with a black dashed line in Fig. 15(c). On the extracted part of the fibre, Y_2O_3 is not detected. However, at the free fibre end, Fig. 15(c) right of the black dashed line, Y_2O_3 sticks to the fibre. The EDS analysis of the interlayer revealed yttrium, oxygen and a small amount of fluorine.

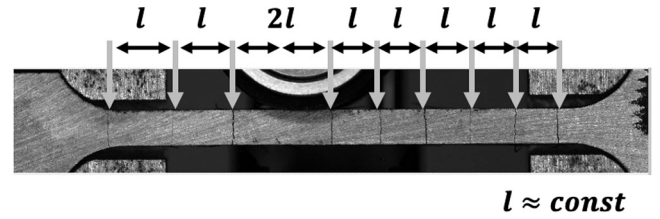


Fig. 16. Multiple matrix cracks of $\text{W}_f/\text{W}_{\text{Y}_2\text{O}_3}$ -TS6 during the tensile test. The distance l of the cracks is approximately constant.

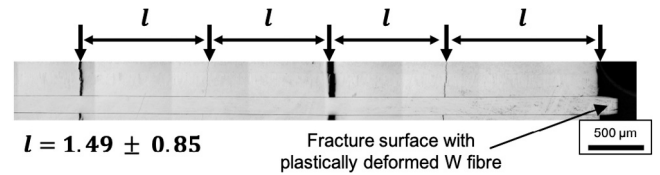


Fig. 17. Multiple matrix failures of $\text{W}_f/\text{W}_{\text{Er}_2\text{O}_3}$ -TS1 after the tensile test. The distance l of the cracks is approximately constant.

4.3. Composite material

The matrix cracking of two bulk $\text{W}_f/\text{W}_{\text{Er}_2\text{O}_3}$ and two bulk $\text{W}_f/\text{W}_{\text{Y}_2\text{O}_3}$ tensile test samples was used for the calculation of the interfacial frictional shear stress. The stress-strain curves of $\text{W}_f/\text{W}_{\text{Er}_2\text{O}_3}$ where previously reported [26] and $\text{W}_f/\text{W}_{\text{Y}_2\text{O}_3}$ showed qualitative the same behaviour. During the loading of the specimens load drops accompanied with an audible cracking noise were observed. For $\text{W}_f/\text{W}_{\text{Y}_2\text{O}_3}$ an optical measurement system for real time displacement evaluation and cracking observation was available and thus the load drops could be correlated to cracking events. For the displacement of $\text{W}_f/\text{W}_{\text{Er}_2\text{O}_3}$ the corrected cross head displacement was used. A good agreement between observed load drops and matrix cracks observed with the optical system and evaluated after the tensile testing was found. Thus, the load drops in the stress-strain curve were attributed to the appearance of a matrix crack. In Fig. 16 a W_f/W tensile specimen with Y_2O_3 during the tensile test is shown. As the specimen is under tensile load, the matrix cracks are open and well visible.

The crack spacing l was measured after the tensile tests with a confocal laser scanning microscopy (CLSM) on both sides of the specimens. A CLSM image for specimen $\text{W}_f/\text{W}_{\text{Er}_2\text{O}_3}$ -TS1 is shown in Fig. 17. This image is representative for all tested material while the crack spacing for $\text{W}_f/\text{W}_{\text{Y}_2\text{O}_3}$ is larger than for $\text{W}_f/\text{W}_{\text{Er}_2\text{O}_3}$.

In Fig. 18 the composite stress over fraction of breaks for the four tested specimens is shown. The stresses for the matrix cracking were indirect determination from the load drops in the load-displacement curves after the experiment.

The investigation of both sides of the specimen was performed to verify if the cracks are recognizable on both sides, thus the matrix is completely broken, which was the case for all samples and cracks. The crack spacing \bar{l} , which is necessary for the calculation of the friction stress is measured. The ultimate tensile strength (UTS) of the specimens, number of cracks, mean values of the crack distances and the fibre ratio are shown in Table 2.

From the values in Fig. 18 and Table 2 the values of τ_{fr} were calculated with Eq. (7) to the following values.

• Er_2O_3 friction:

$$- \tau_{fr-mm-\text{Er}_2\text{O}_3} - \text{TS1} = 48.6 \pm 27.8 \text{ MPa}$$

$$- \tau_{fr-mm-\text{Er}_2\text{O}_3} - \text{TS4} = 52.4 \pm 11.2 \text{ MPa}$$

• Y_2O_3 friction:

$$- \tau_{fr-mm-\text{Y}_2\text{O}_3} - \text{TS4} = 39.2 \pm 17.2 \text{ MPa}$$

Table 2

Listing of the characteristics of the tensile specimens.

Specimen	First load drop [MPa]	UTS [MPa]	Number of cracks	Crack spacing [mm]	Fibre ratio [%]
W _f /W _{Er₂O₃} -TS1	82	482	19	1.49 ± 0.85	22
W _f /W _{Er₂O₃} -TS4	125	557	12	1.63 ± 0.35	22
W _f /W _{Y₂O₃} -TS4	153	235	6	4.24 ± 1.86	11
W _f /W _{Y₂O₃} -TS6	190	251	6	4.52 ± 1.81	11

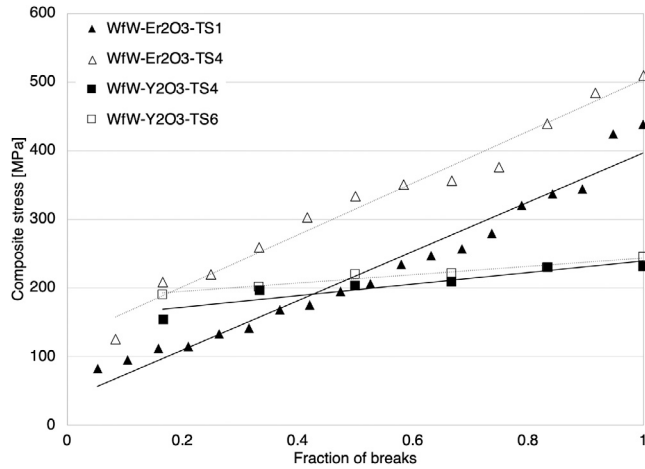


Fig. 18. Composite stress over fraction of breaks. The fracture stress was determined indirect from the occasion of load drops in the stress-strain curves after the experiments.

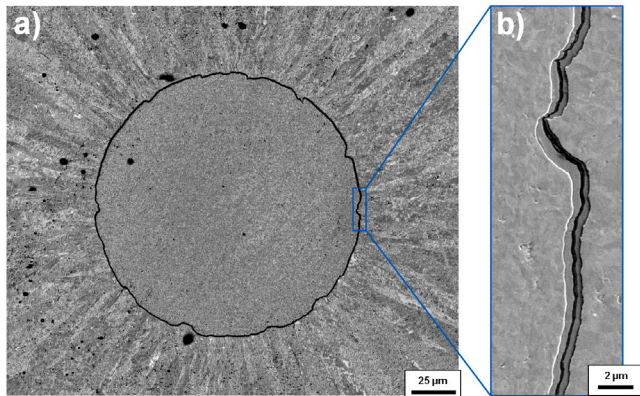


Fig. 19. Top view of the as-fabricated single fibre composite samples with an Er₂O₃ interlayer. The two layered interlayer is also visible in the as fabricated case. The black spot in the middle of the interlayer is only a polishing effect.

$$-\tau_{fr-mm-Y_2O_3} - TS6 = 38.7 \pm 15.5 \text{ MPa}$$

5. Summary and discussion

5.1. Microstructure of the interlayer materials

Single fibre composite samples with Er₂O₃ interlayer show a two-layer interlayer. This can be seen after the push-out test in Fig. 7 and after the pull-out test in Figs. 12 and 13. These two layers are created during the two step PVD process and were also observed in the as-fabricated Er₂O₃ case. A top view on a as-fabricated specimen is shown in Fig. 19.

This process interruption creates an internal interface and the shear stress most likely cause debonding between these two layers. So the Er₂O₃ layer is weaker than the bonding of Er₂O₃ to the fibre or the matrix and Er₂O₃ sticks to the fibre and the matrix.

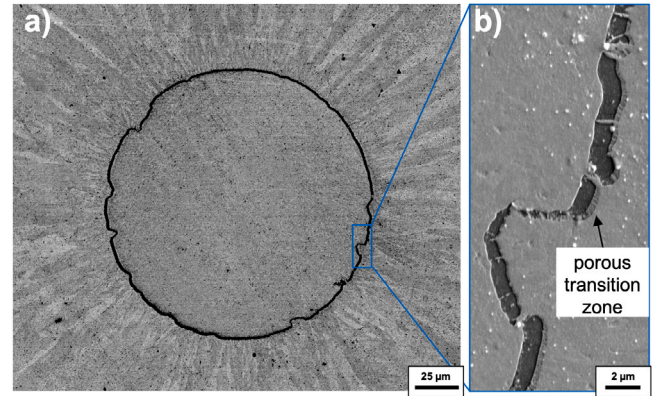


Fig. 20. Top view of the as-fabricated single fibre composite samples with an Y₂O₃ interlayer. The W bridges from the matrix to the fibre and the porous transition zone at the W matrix side can be seen.

The samples with Y₂O₃ interlayer showed W bridges from the matrix through the interlayer to the fibre. The W bridging over the interlayer can be seen in the images in Fig. 8 after the experiments and were also observed in the as fabricated case. The top view on the as-fabricated Y₂O₃ model system is shown in Fig. 20.

Although, the fibres were coated in a two step processes a two-layer system as for Er₂O₃ could not be identified. The Y₂O₃ interlayer debonded between the fibre and the interlayer. This leaves a rough Y₂O₃ surface on the matrix. It indicates that the bonding between the fibre and the Y₂O₃ is weaker than the bonding of the Y₂O₃ to the matrix. One conclusion of that observation is that the internal interface in Er₂O₃ is weaker than the internal interface in Y₂O₃. In addition, the W bridges in the Y₂O₃ could lead to a stabilization of the interlayer and to a strong bonding of the interlayer to the matrix. Thus the debonding took place at the fibre surface and not within the interlayer. However, both materials show a similar debonding behaviour in the force-displacement curves and comparable values, which leads to the conclusion, that the debonding location does not influence the evaluated values.

Thermodynamic calculations with the commercially available software package from CompuTherm LLC, Pandat (CompuTherm LLC, Madison, WI) showed that neither Er₂O₃ nor Y₂O₃ can be considered stable during the W-CVD process. During the deposition with WF₆ the interaction with Er₂O₃ leads to ErF₃ and WO₃ which will be solid below ≈ 850 °C while it gets gaseous above. If Y₂O₃ is used YF₃ and WO₃ will be formed. YF₃ and WO₃ will also be solid below ≈ 850 °C while it gets gaseous above. The Y₂O₃ layers shows a porous transition zone and W bridges after the W-CVD deposition with the used deposition conditions while Er₂O₃ seems to be unaffected. However, previously reported results showed degradation of both interlayer materials after high temperature heat treatment [18]. This indicates that neither Er₂O₃ nor Y₂O₃ can be considered as stable interlayer material in W_f/W and there will be the need for exploring alternatives or adjusting the W deposition conditions e.g. use WCl₆ as precursor.

5.2. Interfacial parameters

A summary of the measured interlayer parameters is shown in Table 3.

Table 3

Summary of the evaluated interlayer parameters and literature values [13].

Method	Interlayer	τ_{deb} [MPa]	τ_{fr} [MPa]	Γ_i [J/m ²]	μ [-]	σ_R [MPa]	$D = \Gamma_i/\Gamma_f$ [-]
Push-out	Er ₂ O ₃	356.2 ± 4.8	180.2 ± 21.3	5.2 ± 0.3	0.62 ± 0.03	290.9 ± 19.8	4.2·10 ⁻⁶
Push-out	Y ₂ O ₃ -1 µm	447.3 ± 2.2	124.6 ± 6.0	5.0 ± 0.2	1.5 ± 0.02	84.1 ± 2.7	4.1·10 ⁻⁶
Push-out	Er ₂ O ₃ -0.6 µm [13]	363 ± 9.0	174 ± 19.5	9.61 ± 1.6	0.64 ± 0.1	272.3 ± 52	8.0·10 ⁻⁶
Push-out	Er ₂ O ₃ -1 µm [13]	399 ± 9.5	64 ± 3.1	2.03 ± 0.2	2.24 ± 0.1	28.7 ± 3.2	1.9·10 ⁻⁶
Pull-out	Er ₂ O ₃	187.3 ± 7.9	154.6 ± 44	3.0 ± 0.65	0.31 ± 0.057	501.2 ± 49	2.5·10 ⁻⁶
Pull-out	Y ₂ O ₃	238.3 ± 11.0	166.6 ± 23	13.0 ± 0.67	0.31 ± 0.026	537.3 ± 29	1.1·10 ⁻⁶
W _f /W	Er ₂ O ₃	–	50.5 ± 19.5	–	–	–	–
W _f /W	Y ₂ O ₃	–	38.9 ± 16.4	–	–	–	–

τ_{deb} evaluated with push-out tests is higher for Y₂O₃ than for Er₂O₃ while τ_{fr} is higher for Er₂O₃ than for Y₂O₃. The specific fracture energies of the interlayers evaluated with the push-out test are similar for both interlayer materials. The largest difference can be seen in the friction coefficient which are 0.62 and 1.5 for Er₂O₃ and Y₂O₃, respectively. The low value for Er₂O₃ is most likely caused by the internal debonding where Er₂O₃ is sliding on Er₂O₃. In contrast to that the high values of Y₂O₃ are caused by the rough surface between fibre and Y₂O₃. The values of τ_{deb} from the previous study [13] are comparable with the values evaluated in the present work (see Table 3). The values of τ_{fr} and Γ_i show a large variation within the previous study as well as within the present evaluation. As the materials are brittle oxide ceramics a large variation is very common based on the weakest link theory [43].

Comparing the results from the pull-out tests it can be seen that τ_{deb} shows higher values for Y₂O₃ than for Er₂O₃ while the τ_{fr} shows only a slight difference. The specific fracture energies of the interlayers show a large difference with a smaller value of 3 J/m² for Er₂O₃ and a higher value of 13 J/m² for Y₂O₃. The much higher Γ_i values for Y₂O₃ could be caused by the bridging W or the limited number of valid tests. The lower values of Er₂O₃ could be caused by the debonding within the layer. The τ_{fr} , determined using the multiple matrix cracking during tensile testing shows ≈ 25% higher values for Er₂O₃ than for Y₂O₃. This could be caused by the different matrix porosity and the slightly different manufacturing process especially the preforms of the tested materials. In general it can be said, that the values for the two different interlayer materials are somehow comparable within the testing methods but decreases from push-out to pull-out test and show the lowest values for the evaluation of the multiple matrix cracking.

As Er₂O₃ and Y₂O₃ are both oxide ceramics with comparable material properties it is no surprise that the interfacial parameters within the testing methods are comparable. However, there are large differences between the individual evaluation methods and the question arises which values represents the behaviour most accurate. Based on the Poisson effect the axial (push-out) force increases the interfacial normal pressure resulting in higher shear stresses. The elastic-plastic indentations occurring at high indenter force of thick specimen lead to a further increase of the interfacial normal pressure. As a result, the forces for the debonding are increased while due to stress relaxation after initial debonding the frictional parameters are unaffected. This results in an overestimation of τ_{deb} and Γ_i . In pull-out tests, the tensile stress on the fibre lead to a elastically strain and thus to a decrease/reduction of the interfacial radial stress. As oxide ceramics are sensitive to tensile loads, this will lead to a lower bonding force as compared to push-out tests. The frictional parameters are not affected as the stress and thus the axial strain on the fibre is decreasing after initial debonding. The τ_{fr} , determined from the multiple matrix cracking of the composite, are much lower than the model system values. In contrast to the model systems, the stress on the fibre is not decreasing after debonding and thus the fibre diameter will be further reduced with increasing load till fracture. This will lead to an underestimation of τ_{fr} . One way to check if the calculated interlayer values from the multiple matrix cracking are reliable is to determine the fracture toughness (K_{Ic}) of the matrix and compare it to literature data. The fracture toughness was calculated by converting Γ_m (Eq. (6)) into K_{Ic} with $K_{Ic} = \sqrt{\Gamma_m/E_m}$ to the following values.

- $K_{Ic-matrix} - TS1(Er_2O_3) = 1.5 \text{ MPa } \sqrt{m}$
- $K_{Ic-matrix} - TS4(Er_2O_3) = 0.9 \text{ MPa } \sqrt{m}$
- $K_{Ic-matrix} - TS4(Y_2O_3) = 9.2 \text{ MPa } \sqrt{m}$
- $K_{Ic-matrix} - TS6(Y_2O_3) = 12.8 \text{ MPa } \sqrt{m}$

The room temperature fracture toughness of CVD W was reported to be around 5 MPa \sqrt{m} [44]. The fracture toughness of polycrystalline tungsten at room temperature ranges from 7 to 15 MPa \sqrt{m} [45]. The matrix fracture toughness of W_f/W_{Er₂O₃} is compared to that relative low while the values for W_f/W_{Y₂O₃} show very good agreement. The low matrix fracture toughness values for the W_f/W_{Er₂O₃} might be caused by the lower density of the matrix of 94% which leads to stress concentration caused by a localized material reduction and thus to premature matrix failure. This leads to more cracks and thus to a lower crack distance which results in a higher evaluated τ_{fr} . In addition, the crack spacing shows a large variation which might be caused by the relative low fibre ratio which does not lead to matrix crack saturation for W_f/W_{Y₂O₃} as it was also seen for other composite materials [46].

Another point which could play a role in the much higher evaluated values from the model systems is residual stress from the manufacturing process. This assumption is based on the different thermal expansion coefficients of the W_f ($4.5 \times 10^{-6} \text{ K}^{-1}$) [3]) and the copper frame ($17 \times 10^{-6} \text{ K}^{-1}$) [47]) on which the fibre was wound. This thermal mismatch leads to tension in the tungsten fibre during the heating to 600 °C during fabrication. Then the W is deposited on the stressed fibres leading to compression in the matrix after cooling the system back to room temperature. This compression acts on the fibres and leading to higher push- and pull-out values. This assumption is not proven yet and residual stress measurements on the same model systems are currently evaluated from high energetic synchrotron x-ray diffraction data.

As a result of the testing method, the evaluated values are largely influenced by the elastic/plastic compression (push-out) or elastic/plastic elongation (pull-out and composite testing) of the fibre. In addition, the manufacturing process which can cause residual stress (single fibre composite) or a different matrix porosity has a large influence on the evaluated values. Piggott [48] proposes to relate the investigation methods of the interlayer to the composite behaviour and, if possible, to produce composite materials with different interlayers and to test them. If this is not possible, the pull-out test is considered to be closer to reality, as it does not compress the interlayer and reproduces the for brittle materials critical tensile load.

5.3. Influence of the evaluated interfacial parameters on W_f/W

The debonding criteria ($D_c = \Gamma_i/\Gamma_f$) for the different experiments are shown in Table 3. The critical ratio D_c of the investigated inter-faces is around 5 orders of magnitudes below the critical value $D_c = 0.25$ [49]. In addition, tensile tests of W_f/W showed that both interlayer materials enable debonding.

Once the fibres are annealed to high temperature Γ_f decreases (see Table 1) and subsequently Γ_i needs to be lower to fulfil the debonding criteria. The maximum Γ_{i-max} values after annealing are shown in Table 4.

Table 4

Γ_{i-max} calculated with $D_c = \Gamma_i/\Gamma_f$ for W fibres after different heat treatment. The values for Γ_f are given in Table 1.

	W_f as-fabricated	W_f annealed 1900 °C for 0.5 h	W_f annealed 2300 °C for 0.5 h	Pure W_f annealed 1627 °C for 0.5 h
Γ_{i-max}	$3.0 \cdot 10^5$ [J/m ²]	$2.4 \cdot 10^5$ [J/m ²]	$5.6 \cdot 10^3$ [J/m ²]	$3.2 \cdot 10^3$ [J/m ²]

Compared to the maximum $\Gamma_i = 13.0$ J/m² for Y₂O₃ (9.6 J/m² [13]) the allowable interlayer fracture energy is over 200 times higher for the pure annealed W_f . Thus it is expected that even after high temperature annealing of W_f/W with decreased fibre properties, fibre debonding will occur. This was also seen in previous experiments of W_f/W were even fully embrittled fibres show debonding in bending tests (interlayer materials: Er₂O₃ and Y₂O₃) [18]. Thus, it is beneficial to have a low Γ_i at the moment which provides a significant safety margin for material changes.

6. Conclusion and outlook

Model systems were used in push- and pull-out tests to investigate the interlayer properties. With these tests, the interfacial shear strength (τ_{deb}), the interfacial frictional shear stress (τ_{fr}) and the specific fracture energy of the interlayer (Γ_i) were determined. In addition, the interfacial frictional shear stress was evaluated from tensile test results of bulk composite. The findings of can be summarized as follows:

1. It was shown that Er₂O₃ and Y₂O₃ can be used as fibre coating in W_f/W as both materials enables fibre–matrix debonding.
2. Influence of the test method is larger than the influence of evaluated interlayer material. (Push-Out: Overestimation of values due to compression, Pull-Out: Elastically diameter reduction prior to debonding, Multiple matrix cracking: Large influence of material (porosity, fibre ratio).)
3. If the aim is material screening or to get input parameters for modelling the pull-out test should be used as all necessary interlayer parameters can be evaluated with tensile loading (critical load in real composite materials).
4. It is expected that the due to high Γ_f in the as-fabricated case, debonding is possible for nearly any interlayer material. Even after fibre annealing, the fibres provides a significant design space for the interlayer development which is beneficial for covering irradiation induced material change.

As it was shown, a alternative to Er₂O₃ and Y₂O₃ needs to be found as interlayer material. Recently performed thermodynamic calculations for ZrO₂ showed that an increased H flow during the deposition will at least for ZrO₂ prevent any interaction during the deposition. The calculations showed, that ZrO₂ has a higher resistances against the harsh depositions conditions and might be a useful alternative.

Another topic which needs to be addressed in future work is the material changes which will take place during neutron irradiation, as neutron irradiation has the potential to significantly decrease Γ_f in combination with material swelling. Material swelling might result in a increasing Γ_i due to compression on the interlayer. Thus, this changes needs to be taken into account for the further development of W_f/W .

CRediT authorship contribution statement

H. Gietl: Conceptualization, Methodology, Investigation, Visualization, Formal analysis, Writing – original draft. **J. Riesch:** Conceptualization, Supervision, Writing – review & editing. **M. Zielinski:** Investigation. **T. Höschen:** Resources, Methodology. **J.W. Coenen:** Resources, Writing – review & editing. **S. Schönen:** Writing – review & editing. **R. Neu:** Funding acquisition, Supervision, Writing – review & editing.

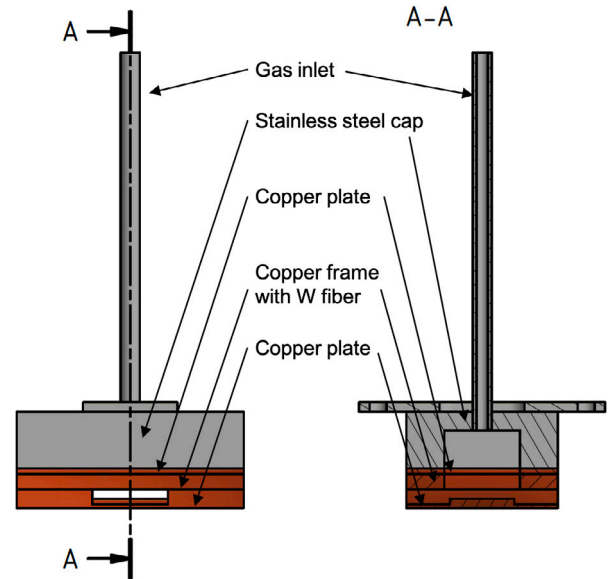


Fig. A.1. Technical drawing of the set up for the fabrication of the single fibre composites.

Declaration of competing interest

The authors declare that they have no known competing financial interests or personal relationships that could have appeared to influence the work reported in this paper.

Acknowledgements

The authors want to acknowledge the Osram GmbH, Schwabmünchen, Germany for providing the W wire and the whole W_f/W team for the fruitful collaboration. I also thank Ying Yang from the Oak Ridge National Laboratory. This work has been carried out within the framework of the EUROfusion Consortium and has received funding from the Euratom research and training programme 2014–2018 and 2019–2020 under grant agreement No 633053. The views and opinions expressed herein do not necessarily reflect those of the European Commission. Research sponsored by the U.S. Department of Energy, Office of Fusion Energy Sciences, under contract DE-AC05-00OR22725 with UT-Battelle, LLC.

Appendix

A technical drawing of the set up for the manufacturing of the pull-out and push-out specimens is shown in Fig. A.1.

References

- [1] V. Philipps, Tungsten as material for plasma-facing components in fusion devices, *J. Nucl. Mater.* 415 (1) (2011) 2–9.
- [2] C. Gandhi, M.F. Ashby, Overview no. 5: Fracture-mechanism maps for materials which cleave: F.C.C., B.C.C. and H.C.P. metals and ceramics, *Acta Metall.* 27 (10) (1979) 1565–1602.
- [3] E. Lassner, W.-D. Schubert, Tungsten - Properties, Chemistry, Technology of the Element, Alloys, and Chemical Compound, Springer, 1999.

- [4] W. Yih, C. Wang, Tungsten: Sources, Metallurgy, Properties, and Applications, Springer US, 1979.
- [5] V. Barabash, G. Federici, M. Rödiger, L. Snead, C. Wu, Neutron irradiation effects on plasma facing materials, *J. Nucl. Mater.* 283–287 (2000) 138–146.
- [6] J.M. Steichen, Tensile properties of neutron irradiated TZM and tungsten, *J. Nucl. Mater.* 60 (1976) 13–19.
- [7] Ch. Linsmeier, M. Rieth, J. Aktaa, T. Chikada, A. Hoffmann, J. Hoffmann, A. Houben, H. Kurishita, X. Jin, M. Li, et al., Development of advanced high heat flux and plasma-facing materials, *Mater. Sci. Eng. A* 57 (9) (2018) 092007.
- [8] R. Neu, J. Riesch, A.v. Müller, M. Balden, J.W. Coenen, H. Gietl, T. Höschchen, M. Li, S. Wurster, J.-H. You, Tungsten fibre-reinforced composites for advanced plasma facing components, *Nucl. Mater. Energy* 12 (2016) 1308–1313.
- [9] Y. Mao, J.W. Coenen, J. Riesch, S. Sistla, J. Almannstötter, B. Jasper, A. Terra, T. Höschchen, H. Gietl, M. Bram, J. Gonzalez-Julian, C. Linsmeier, C. Bröckmann, Development and characterization of powder metallurgically produced discontinuous tungsten fiber reinforced tungsten composites, *Phys. Scr. (T170)* (2017) 014005.
- [10] A.G. Evans, F.W. Zok, The physics and mechanics of fibre-reinforced brittle matrix composites, *J. Mater. Sci.* 29 (1994) 3857–3896.
- [11] J. Riesch, J. Almannstötter, J.W. Coenen, M. Fuhr, H. Gietl, Y. Han, T. Höschchen, Ch. Linsmeier, N. Travitzky, P. Zhao, Properties of drawn wire used as high performance fibre in tungsten fibre-reinforced tungsten composite, *IOP Conf. Ser.: Mater. Sci. Eng.* 136 (2016) 012043.
- [12] J. Riesch, Y. Han, J. Almannstötter, J.W. Coenen, T. Höschchen, B. Jasper, P. Zhao, Ch. Linsmeier, R. Neu, Development of tungsten fibre-reinforced tungsten composites towards their use in DEMO - potassium doped tungsten wire, *Phys. Scr. T167* (2016) 014006.
- [13] J. Du, A Feasibility Study of Tungsten-Fiber-Reinforced Tungsten Composites with Engineered Interfaces (PhD thesis), Technische Universität München, 2010.
- [14] J. Du, T. Höschchen, M. Rasinski, S. Wurster, W. Grosinger, J.-H. You, Feasibility study of a tungsten wire-reinforced tungsten matrix composite with ZrOx interfacial coatings, *Compos. Sci. Technol.* 70 (2010) 1482–1489.
- [15] H. Gietl, A.v. Müller, J. Riesch, J.W. Coenen, T. Höschchen, Ph. Huber, M. Decius, D. Ewert, M. Milwich, R. Neu, Textile techniques for tungsten fibre-reinforced composites production, *J. Compos. Mater.* 52 (28) (2018) 3875–3884.
- [16] H. Gietl, J.W. Riesch, J.W. Coenen, T. Höschchen, R. Neu, Production of tungsten-fibre reinforced tungsten composite by a novel continuous chemical vapour deposition process, *Fusion Eng. Des.* 146 (2019) 1426–1430.
- [17] J. Riesch, J.Y. Buffiere, T. Höschchen, M. Scheel, Ch. Linsmeier, J.-H. You, Crack bridging in as-fabricated and embrittled tungsten single fibre-reinforced tungsten composites shown by a novel in-situ high energy synchrotron tomography bending test, *Nucl. Mater. Energy* 15 (2018) 1–12.
- [18] H. Gietl, S. Olbrich, J. Riesch, G. Holzner, T. Höschchen, J.W. Coenen, R. Neu, Estimation of the fracture toughness of tungsten fibre-reinforced tungsten composites, *Eng. Fract. Mech.* (2020) 107011.
- [19] Stephan Schönen, Bruno Jasper, Jan Willem Coenen, Juan Du, Till Höschchen, Johann Riesch, Ghaleb Natour, Rudolf Neu, Christian Linsmeier, Insight into single-fiber push-out test of tungsten fiber-reinforced tungsten, *Compos. Interfaces* 26 (2) (2019) 107–126.
- [20] J. Du, T. Höschchen, M. Rasinski, J.-H. You, Shear debonding behavior of a carbon-coated interface in a tungsten fiber-reinforced tungsten matrix composite, *J. Nucl. Mater.* 417 (2011) 472–476.
- [21] J. Du, T. Höschchen, J.-H. You, Thermal stability of the engineered interfaces in W_f/W composites, *J. Mater. Sci.* 47 (2012) 4706–4715.
- [22] B. Jasper, S. Schönen, J. Du, T. Höschchen, F. Koch, C. Linsmeier, R. Neu, J. Riesch, A. Terra, J.W. Coenen, Behavior of tungsten fiber-reinforced tungsten based on single fiber push-out study, *Nucl. Mater. Energy* 9 (2016) 416–421.
- [23] P. Zhao, J. Riesch, T. Höschchen, J. Almannstötter, M. Balden, J.W. Coenen, U. Himml, U. von Toussaint, R. Neu, Microstructure, mechanical behavior and fracture of pure tungsten wires after different heat treatments, *Int. J. Refract. Met. Hard Mater.* 68 (2017) 29–40.
- [24] J. Riesch, M. Aumann, J.W. Coenen, H. Gietl, G. Holzner, T. Höschchen, P. Huber, M. Li, Ch. Linsmeier, R. Neu, Chemically deposited tungsten fibre-reinforced tungsten - The way to a mock-up for divertor applications, *Nucl. Mater. Energy* 9 (2016) 75–83.
- [25] L. Raumann, J.W. Coenen, J. Riesch, Y. Mao, H. Gietl, T. Höschchen, Ch. Linsmeier, O. Guillon, Modeling and validation of chemical vapor deposition of tungsten for tungsten fiber reinforced tungsten composites, *Surf. Coat. Technol.* 381 (2020) 124745.
- [26] H. Gietl, J. Riesch, J.W. Coenen, T. Höschchen, C. Linsmeier, R. Neu, Tensile deformation behavior of tungsten fibre-reinforced tungsten composite specimens in as-fabricated state, *Fusion Eng. Des.* 124 (2016) 396–400.
- [27] L.B. Greszczuk, Interfaces in Composites, American Society of Testing and Materials, 1968, pp. 42–58.
- [28] L. Greszczuk, Theoretical studies of the mechanics of the fiber-matrix interface in composites, in: *Interfaces in Composites*, ASTM International, 1969.
- [29] P. Lawrence, Some theoretical considerations of fibre pull-out from an elastic matrix, *J. Mater. Sci.* 7 (1) (1972) 1–6.
- [30] R.J. Gray, Analysis of the effect of embedded fibre length on fibre debonding and pull-out from an elastic matrix, *J. Mater. Sci.* 19 (3) (1984) 861–870.
- [31] D.K. Shetty, Shear-lag analysis of fiber push-out (indentation) tests for estimating interfacial friction stress in ceramic-matrix composites, *J. Am. Ceram. Soc.* 71 (2) (1988) C-107.
- [32] C. Liang, J.W. Hutchinson, Mechanics of the fiber pushout test, *Mech. Mater.* 14 (3) (1993) 207–221.
- [33] A. Takaku, R.G.C. Arridge, The effect of interfacial radial and shear stress on fibre pull-out in composite materials, *J. Phys. D: Appl. Phys.* 6 (17) (1973) 2038.
- [34] John W. Hutchinson, Henrik M. Jensen, Models of fiber debonding and pullout in brittle composites with friction, *Mech. Mater.* 9 (2) (1990) 139–163.
- [35] Matthew Newville, Till Stensitzki, Daniel B. Allen, Michal Rawlik, Antonino Ingargiola, Andrew Nelson, LMFIT: Non-linear Least-Square Minimization and Curve-Fitting for Python, Ascl, 2016, pp. ascl-1606.
- [36] J. Aveston, G.A. Cooper, A. Kelly, The Properties of Fibre Composites, IPC Science and Technology Press, 1971.
- [37] W.A. Curtin, Multiple matrix cracking in brittle matrix composites, *Acta Metall. Mater.* 41 (5) (1993) 1369–1377.
- [38] A.G. Evans, F.W. Zok, J. Davis, The role of interfaces in fiber-reinforced brittle matrix composites, *Compos. Sci. Technol.* 42 (1991) 3–24.
- [39] B. Budiansky, J.W. Hutchinson, A.G. Evans, Matrix fracture in fiber-reinforced ceramics, *J. Mech. Phys. Solids* 34.2 (1986) 167–189.
- [40] D.B. Marshall, B.N. Cox, A.G. Evans, The mechanics of matrix cracking in brittle matrix fiber composites, *Acta Metall.* 33 (1985) 2013–2021.
- [41] R.-Y. Kim, N.J. Pagano, Crack initiation in unidirectional brittle-matrix composites, *J. Am. Ceram. Soc.* 74 (5) (1991) 1082–1090.
- [42] J.-K. Kim, C. Baillie, Y.-W. Mai, Interfacial debonding and fibre pull-out stresses, *J. Mater. Sci.* 27 (1991) 3143–3154.
- [43] J.B. Wachtman, W.R. Cannon, M.J. Matthewson, Mechanical Properties of Ceramics, second ed., 2009.
- [44] J.D. Murphy, A. Giannattasio, Z. Yao, C.J.D. Hetherington, P.D. Nellist, S.G. Roberts, The mechanical properties of tungsten grown by chemical vapour deposition, *J. Nucl. Mater.* 386–388 (2009) 583–586.
- [45] E. Gaganidze, D. Rupp, J. Aktaa, Fracture behaviour of polycrystalline tungsten, *J. Nucl. Mater.* 446 (2014) 240–245.
- [46] Gregory N. Morscher, Julian Martinez-Fernandez, Mark J. Purdy, Determination of interfacial properties using a single-fiber microcomposite test, *J. Am. Ceram. Soc.* 79 (4) (1996) 1083–1091.
- [47] Joseph R. Davis, et al., Copper and Copper Alloys, ASM international, 2001.
- [48] M.R. Piggott, Why interface testing by single-fibre methods can be misleading, *Compos. Sci. Technol.* 57 (8) (1997) 965–974.
- [49] M.-Y. He, J.W. Hutchinson, Crack deflection at an interface between dissimilar elastic materials, *Int. J. Solids Struct.* 25 (1989) 1053–1067.